ANNALS OF
BOTANY
Founded 1887

Assessing radiation dose limits for X-ray fluorescence microscopy analysis of plant specimens

Michael W. M. Jones[1,*], Peter M. Kopittke[2], Lachlan Casey[3], Juliane Reinhardt[4,†], F. Pax C. Blamey[2] and Antony van der Ent[5]

[1]*Central Analytical Research Facility, Institute for Future Environments, Queensland University of Technology, Australia,*
[2]*School of Agriculture and Food Sciences, The University of Queensland, Australia,* [3]*Centre for Microscopy and Microanalysis,*
The University of Queensland, Australia, [4]*Australian Synchrotron, ANSTO, Australia and* [5]*Sustainable Minerals Institute, The*
University of Queensland, Australia
[†]*Present address: Advanced Light Source, Lawrence Berkeley National Laboratory, 1 Cyclotron Rd, Berkeley, CA 94720, USA*
For correspondence. E-mail mw.jones@qut.edu.au

• **Background and Aims** X-ray fluorescence microscopy (XFM) is a powerful technique to elucidate the distribution of elements within plants. However, accumulated radiation exposure during analysis can lead to structural damage and experimental artefacts including elemental redistribution. To date, acceptable dose limits have not been systematically established for hydrated plant specimens.
• **Methods** Here we systematically explore acceptable dose rate limits for investigating fresh sunflower (*Helianthus annuus*) leaf and root samples and investigate the time–dose damage in leaves attached to live plants.
• **Key Results** We find that dose limits in fresh roots and leaves are comparatively low (4.1 kGy), based on localized disintegration of structures and element-specific redistribution. In contrast, frozen-hydrated samples did not incur any apparent damage even at doses as high as 587 kGy. Furthermore, we find that for living plants subjected to XFM measurement *in vivo* and grown for a further 9 d before being reimaged with XFM, the leaves display elemental redistribution at doses as low as 0.9 kGy and they continue to develop bleaching and necrosis in the days after exposure.
• **Conclusions** The suggested radiation dose limits for studies using XFM to examine plants are important for the increasing number of plant scientists undertaking multidimensional measurements such as tomography and repeated imaging using XFM.

Key Words: Sunflower (*Helianthus annuus*), X-ray fluorescence microscopy, radiation damage, radiation dose.

INTRODUCTION

X-ray fluorescence microscopy (XFM) is a powerful technique that allows sub-micron scale mapping of endogenous and exogenous elements in plant specimens (de Jonge and Vogt, 2010; de Jonge *et al.*, 2010; Lombi *et al.*, 2011; Hare *et al.*, 2015; Hackett *et al.*, 2019). XFM can provide information on elemental distribution, not only *in situ* but also *in vivo* (Scheckel *et al.*, 2004; Blamey *et al.*, 2018). Elucidating the cellular and tissue-level distribution of elements is, however, inherently challenging, and XFM necessitates strict requirements on specimen collection, preparation and analytical conditions, in order to avoid elemental redistribution and ultrastructural alterations, and to be able to accurately report 'life-like' elemental distribution, concentration and co-ordination chemistry (van der Ent *et al.*, 2017; Kopittke *et al.*, 2018). Ideally, specimens are analysed 'as is' in their natural hydrated state without any method of preservation. However, practical considerations such as specimen availability and transport can render this unfeasible in some situations. Freeze-drying (lyophilization) or cryogenic preservation of specimens are acceptable alternatives to the ideal, if properly performed (van der Ent *et al.*,

2017). Chemical fixation, on the other hand, has to be avoided, as it invariably causes catastrophic elemental redistribution (Turnau *et al.*, 2001; Budka *et al.*, 2004). Similarly, no freeze-substitution protocol fully preserves *in situ* elemental distribution (Budka *et al.*, 2004, 2005; Kachenko *et al.*, 2008).

When studying sensitive systems, it is critical to ensure that specimen integrity is maintained throughout the period of measurement itself. The X-rays necessary to excite fluorescence interact with the specimen, and can themselves potentially cause changes. Mass loss, changes in the specimen ultrastructure (Weiß *et al.*, 2000; Larabell and Le Gros, 2004; Kosior *et al.*, 2012), bond breaking (Beetz and Jacobsen, 2002; Gianoncelli *et al.*, 2015) and element redistribution (James *et al.*, 2016; Jones *et al.*, 2017) have all been reported and must be managed. Recent advances in detector efficiency and associated processing methods (Ryan *et al.*, 2014, 2018; Siddons *et al.*, 2014) have reduced the required radiation dose to the point where living plants (van der Ent *et al.*, 2017; Blamey *et al.*, 2018; Doolette *et al.*, 2018) or excised hydrated plant organs such as roots or leaves (Kopittke *et al.*, 2011; Li *et al.*, 2019) can be imaged without radiation-protective

sample preparation. However, care must still be taken when imaging biological specimens in their native state to ensure no radiation damage has occurred (Lombi *et al.*, 2011; James *et al.*, 2016).

A change made by the act of observation on a system being investigated is often referred to as an observer effect (Hare *et al.*, 2015; Jones *et al.*, 2017). When small, the effect may accumulate and introduce subtle but significant system-wide errors, while large effects may simply preclude analysis. Within cells and tissues, elements are diffusible, bound in complexes or as precipitates, leading to possible differences in the dose thresholds, with gross morphological changes probably occurring at different dose thresholds to intracellular effects. There is therefore a need for optimal parameters to be defined for individual elements. The development of radiation dose limits, below which specimen integrity can be maintained and element distributions within the specimen are unaffected, is necessary to ensure valid interpretations. Previous work by Jones *et al.* (2017) defined a set of element-specific radiation dose limits in the nematode *Caenorhabditis elegans*, and suggest limits for three chemical-free preparations: live, lyophilized and cryogenically frozen. However, it is likely that such limits vary by organism, and while these suggested limits appear to apply to many biological specimens (James *et al.*, 2016; Hackett *et al.*, 2019), there is evidence that radiation-induced damage manifests at a far lower radiation dose in plant specimens in the order of 200 kGy (Lombi *et al.*, 2011). In the latter case, radiation-induced metal redistribution occurred during a tomographic series after recording 75 out of a total of 100 projections, or after a time of approx. 225 min (Lombi *et al.*, 2011). The authors report that they 'were able to beat the onset of radiation damage' by collecting 2-D tomographic slices rather than a 3-D tomographic volume, reducing the total measurement time to <15 min compared with the 5 h required for 100 projections, despite increasing the effective per-pixel dwell and therefore increasing the effective per-pixel radiation dose delivered to the specimen (Lombi *et al.*, 2011). This result suggests that for a living plant specimen, measurement time plays an important role in limiting the observer effect.

There is an increasing ability of XFM beamlines also to conduct experiments where the specimen is scanned multiple times, thereby increasing the dose. For example, both tomography and fluorescence X-ray absorption near edge structure imaging (XANES imaging) may result in the specimen being scanned up to 100 times during the analysis (Lombi *et al.*, 2011; Kopittke *et al.*, 2014). As the level of radiation dose increases, the specimen suffers from cellular damage and eventual elemental redistribution, which can render interpretation problematic (van der Ent *et al.*, 2017). For example, Scheckel *et al.* (2004) studied leaves of *Iberis intermedia in vivo*, stating 'we observed slight beam-induced damage of the *I. intermedia* leaf tissue after μ-XRF mapping'. Whether this damage had caused elemental redistribution is unknown. Damage has also been reported using in-house XFM. For example, Fittschen *et al.* (2017) reported 'severe damage to the regions exposed to radiation' but, again, it is unknown whether this affected elemental distribution in the specimen.

In the present study, we extend previous work on *C. elegans* (Jones *et al.*, 2017) to leaves and roots of sunflower

(*Helianthus annuus*), both recently excised (i.e. fresh hydrated) and cryogenically frozen. These tissues were chosen as models because of their high hydration, ostensibly making them highly susceptible to radiation-induced damage, allowing the results from this study to be conservatively applied to all plant specimens. In addition, we explored the time dependence of radiation-induced damage. The objectives of this study were 3-fold: (1) to determine dose limits for investigating fresh sunflower leaf and root specimens; (2) to compare the results obtained from live/fresh plant specimens with those exposed in the frozen-hydrated state; and (3) to investigate the influence of time on radiation damage in live plants.

MATERIALS AND METHODS

Plant specimen preparation

Rolled paper towels with sunflower (cv. Ausiegold 62) seeds were placed in tap water and seedlings were transplanted 4 d later into 20 L pots of aerated nutrient solution at pH 5.6 and an ionic strength of approx. 3 mм (Blamey *et al.*, 2015) similar to that in soil solutions (Kopittke *et al.*, 2010). Nominal concentrations of nutrients in the basal solution were 1000 μм Ca, 120 μм NH_4^+-N, 95 μм Mg, 300 μм K, 10 μм Na, 6 μм Fe, 0.2 μм Mn, 0.5 μм Zn, 0.2 μм Cu, 1250 μм Cl, 670 μм NO_3-N, 340 μм S, 20 μм P, 1.0 μм B and 0.01 μм Mo. Plants were kept in a controlled environment room at 25 °C under high-pressure sodium lamps with photosynthetically active radiation of approx. 1500 μmol m^{-2} s^{-1} measured at canopy height. After 7 d, 0.92 mL of 0.065 м $MnSO_4$ was added to each pot (equivalent to 30 μм Mn in nutrient solution), and a further 2.6 mL of 0.031 м KH_2PO_4 per pot were added daily (equivalent to 4 μм P in nutrient solution) to ensure adequate P supply. Plants were transferred to the Australian Synchrotron and grown in fresh nutrient solutions at 22 °C under high-pressure sodium lights.

Synchrotron-based XFM

The XFM beamline of the Australian Synchrotron (Clayton, Australia) employs an in-vacuum undulator to produce a brilliant X-ray beam of 4.1–20 keV (flux up to 4.0×10^{11} photons s^{-1}) with a focus down to approx. 1 μm. A Si(111) monochromator and a Kirkpatrick–Baez (KB) pair of mirrors deliver a monochromatic focused beam onto the specimen (Paterson *et al.*, 2011). X-ray fluorescence photons were collected using a Maia detector (Revision D) (Kirkham *et al.*, 2010; Siddons *et al.*, 2014) placed in the backscatter geometry with spectra analysed using GeoPIXE (Ryan *et al.*, 2002).

In-house XFM

The microXRF facility at The University of Queensland (St Lucia, Australia) is a modified IXRF ATLAS X system, with a XOS FleX beam 50 W microfocus Mo-target source producing 17.4

KeV X-rays (flux of 2.2×10^8 photons s^{-1}) at a spot size of 25 µm, and two 150 mm^2 KETEK VITUS CUBE SDDs (with a 25 µm Be-window), coupled to a XIA Mercury X4 signal processing unit.

Specimen mounting for XFM analysis

Samples at the Australian Synchrotron were mounted in three different ways depending upon the analysis. First, for analyses of excised tissues at room temperature, whole leaves were excised from the living donor plant immediately before the analysis and held between two sheets of polypropylene thin film (4 µm thickness) stretched over a Perspex frame magnetically attached to the *x–y* motion stage at atmospheric temperature (approx. 25 °C). The petiole of the leaf was inserted into a small pouch with paper soaked in nutrient solution to ensure that the leaf remained turgid, with the polypropylene film that completely sealed the leaf also helping to ensure that it did not dehydrate. Fresh roots, approx. 2 cm long, were excised, placed between two sheets of polypropylene thin film, and pouches with nutrient solution-soaked paper were placed at both ends of the root.

For cryogenic analysis at the Australian Synchrotron, small specimens (approx. 1×2 cm) were cut from whole leaves and mounted onto a flat carbon planchette pole (by gluing the lower end onto the carbon pole with cyanoacrylate glue) before being driven into a stream of N$_2$ at approx. –100 °C. Similarly, roots (cut to approx. 2 cm long) were mounted in a hollow carbon tube by inserting one end. The freezing was rapid (<1 s), although not sufficiently rapid to affect vitreous ice formation (Warley, 1997). Diffraction from ice crystals was not observed in the Maia detector, leading us to conclude that any ice crystals that had formed were too small (i.e. sub-cellular scale) to be problematic for the scale of the investigation here.

Living plants were mounted whole in custom-designed specimen holders at the Australian Synchrotron (Blamey *et al.*, 2018). Briefly, the Perspex holder had a 50 mL polypropylene centrifuge tube (30×115 mm) attached to it, in which the roots of the plant were submerged in 40 mL of basal nutrient solution. Securing the plant stem in the neck of the tube by rolling a length of 15 mm wide Parafilm M® prevented solution spillage onto sensitive beamline equipment. The plant itself was mounted as described above for the whole excised (fresh hydrated) leaves. Immediately after the experiment, the leaves were imaged using light microscopy and the plants were returned to the nutrient solution culture conditions and later to the controlled-environment room described above. The leaves were imaged daily using light microscopy. In-house XFM measurements were performed 9 d after the initial synchrotron-based XFM measurements. The previously imaged leaves were excised from the living donor plant, and again mounted between polypropylene thin films, as for the synchrotron-based experiments described earlier.

X-ray-induced damage assessment

The aim of this experiment was to expose plant specimens to increasing doses to establish their sensitivity to X-ray damage. The different specimen types and preparations,

excised hydrated leaves, cryogenically fixed hydrated leaves, excised hydrated roots and cryogenically fixed hydrated roots ($n = 3, 2, 2$ and 2, respectively), were all imaged on the XFM beamline at the Australian Synchrotron using a 15.6 keV incident beam focused to approx. 2.5 µm full width at half-maximum (FWHM; 1.1 µm 1σ) at the specimen. The flux delivered to the specimen with a secondary source aperture (SSA) size of 50 ìm horizontal by 200 µm vertical was approximately equal to 9.9×10^9 photons s^{-1}. To alter the dose delivered to the various specimens, the beam intensity was adjusted by varying the SSA horizontal size in the range from 10 to 300 µm. The incident flux was measured with a calibrated ion chamber placed after the SSA, providing an accurate measure of the flux delivered to the specimen for each scan. In addition to varying the beam intensity using the SSA, the speed of the scanning stage (and therefore the effective dwell per pixel) was also varied from 5 µm s^{-1} to 4 mm s^{-1}. A sampling interval of 2 µm in both the horizontal and vertical direction oversampled the beam spot, yielding a final image resolution approaching 2 µm.

To assess the cumulative radiation-induced damage, we performed a 'damage loop' (Fig. 1) as described previously (Beetz and Jacobsen, 2002; Jones *et al.*, 2017). The reference image was collected with minimal dose (approx. 200 Gy) over an area of approx. 1 mm^2 for each specimen type and preparation, with the damage image collected over approximately half this area, with an increasing dose for each loop. Five reference images (total cumulative dose approx. 1.2 kGy over about 25 min) were collected before the damage loop was initialized to provide sufficient statistics to condition the data for analysis as described previously (Jones *et al.*, 2017).
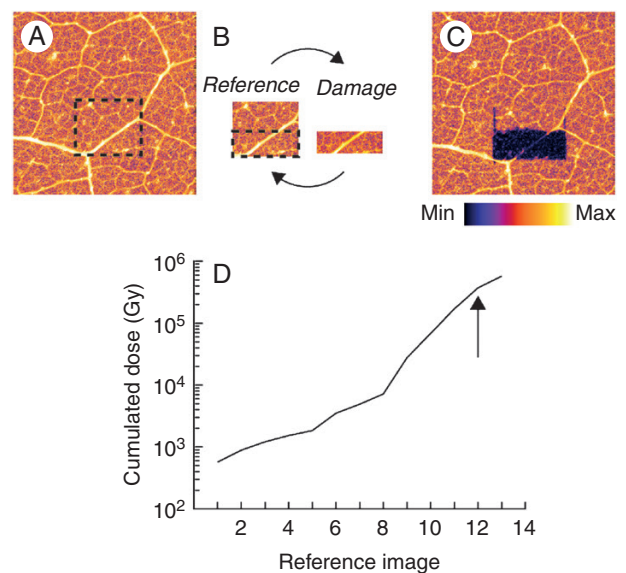

Fig. 1. Schematic of the experimental damage loop. An initial overview area was imaged (A) from which a smaller reference image was selected (B – reference) and a smaller damaged area within the reference image (B – damage). The reference and damage image pair constitute the 'damage loop'. Following the damage loop, a final overview area was imaged (C). The cumulated dose at each reference image is shown in (D). The arrow in (D) indicates the reference image where measurements were stopped.

To assess the effect of time on radiation-induced damage *in vivo* using living plants, four individual plants were mounted and a single selected leaf was delivered a radiation dose (0.3, 0.9, 3 or 8 kGy) over an area of approx. 1 cm^2. The area was imaged optically immediately following the radiation dose delivery and at regular time intervals afterwards up to 9 d while plants remained in nutrient solution. After 9 d, the same area was imaged via the in-house XFM at The University of Queensland to determine elemental changes as a result of the initial radiation dose.

Dose estimation

Radiation dose is the measure of the energy deposited per unit mass of specimen. Here, we estimate the X-ray imaging dose (*D*) from the total X-ray interaction cross-section (Kirz *et al.*, 1995) as:

$$D = \frac{I_0 t E}{A} \left[\frac{\mu}{\rho} \right] \quad (1)$$

where I_0 is the incident photon intensity, *E* is the photon energy, $\left[\frac{\mu}{\rho} \right]$ is the X-ray mass attenuation coefficient, *t* is the measurement time and *A* is the sampling area. It is worth noting that the X-ray mass attenuation coefficient is X-ray energy dependent, rapidly decreasing as a function of energy. In the case presented here, we oversampled a 2.5 µm focus spot with 2 × 2 µm pixels, reducing the sampling area to the pixel size, and the measurement time to the effective per-pixel dwell. Furthermore, we approximated the specimen composition as hydrated cellulose, with an empirical formula of $(H_2O)_{90}C_6H_{10}O_5$ and an X-ray mass attenuation coefficient of 1.48 cm^2 g^{-1} at 15.6 keV. For a detailed discussion of radiation dose estimation, including the energy and composition dependence and the errors involved, we encourage the reader to read Jones *et al.* (2017) and the supplementary information contained therein.

Damage assessment

Radiation-induced damage was assessed using the method developed by Jones *et al.* (2017). Briefly, the reference images were aligned using an intensity-based image alignment method to the first image of the series, and the first five reference images were used to determine the intrinsic element-specific variability of the mean (μ_i) and s.d. (σ_i) of the measurement at each pixel (subscript *i*) and to condition the s.d. (σ_i) to ensure that subsequent analysis is not dominated by local underestimates of the s.d. (Jones *et al.*, 2017). Any change in the recorded X-ray signal in any pixel for each dose can then be estimated using the χ^2 metric:

$$\chi_i^2 (D) = \left(\frac{Q_i (D) - \mu_i}{\sigma_i} \right)^2 \quad (2)$$

where $Q_i(D)$ is the recorded X-ray signal at each pixel *i* for each dose *D*. To estimate the change for each specimen, we compared the sum of the χ^2 described in eqn (2) for the area of

the reference image that was damaged (*d*) compared with the undamaged control area (*c*) and average it over *n* specimens to obtain a quantification of radiation-induced damage as a function of radiation dose (Jones *et al.*, 2017):

$$\overline{\chi_X^2} = \frac{1}{n} \sum_n \chi_X^2 = \frac{1}{n} \sum_n \frac{\chi_d^2}{\chi_c^2} = \frac{1}{n} \sum_n \frac{\overline{\chi_{i,d}^2 (D)}}{\overline{\chi_{i,c}^2 (D)}} \quad (3)$$

The cumulative radiation-induced damage is assessed using a 'damage loop' (Fig. 1) as described previously (Beetz and Jacobsen, 2002; Jones *et al.*, 2017), which allows a statistical assessment of the radiation-induced damage to the specimen to be calculated.

RESULTS

Plots of the mean of the normalized global image change metric $\bar{\chi}_X^2 (D)$ [eqn (3)] for each measured analyte as a function of cumulative radiation dose (Gy) for excised hydrated leaves, excised cryogenic hydrated leaves, excised hydrated roots and excised cryogenic hydrated roots are presented in Fig. 2, with an example final reference image for each specimen type. Here, we tracked the damage per element as a function of radiation dose up to 0.4 MGy (hydrated specimens) and up to 0.6 MGy (cryogenic specimens). We find that elemental-specific radiation damage occurs in excised hydrated specimens (Fig. 2A, C) at a significantly lower dose than reported for biological specimens (Jones *et al.*, 2017), while no damage is observed in excised cryogenically frozen specimens (Fig. 2B, D), in line with previously reported observations for different specimen types (Beetz and Jacobsen, 2002; Jones *et al.*, 2017). The damage thresholds are summarized in Table 1, together with a comparison with previous work on *C. elegans* (Jones *et al.*, 2017).

We understand that few researchers measure or report the radiation dose delivered to the specimen during an XFM experiment, instead reporting experimental parameters such as dwell and pixel size. To aid the general reader, Table 2 gives approximate conversions for different synchrotron facilities for hydrated plants at an energy of 15 keV (k-alpha used for the Mo source for the in-house microscope). This allows estimation for different conditions to approximate their dose. Using eqn (1) as a guide, dose is proportional to the flux and dwell time, and inversely proportional to the pixel area (pixel size^2), therefore, dose can be minimized by reducing either flux or dwell time, or increasing the beam spot and pixel size.

Radiation damage in excised (hydrated) leaves

In excised hydrated leaves, the observed damage is element specific, with more diffusible elements being more susceptible (K > Ca > Mn > Zn) (Fig. 2A, C). The progression of the radiation-induced damage is presented in Fig. 3, highlighting the elemental-specific damage shown in Fig. 2. Elemental maps of Ca, Mn and K together with maps of the $\chi^2(D)$ at two accumulated radiation dose levels for the same elements show changes in the specimen for both Ca and Mn at a dose level
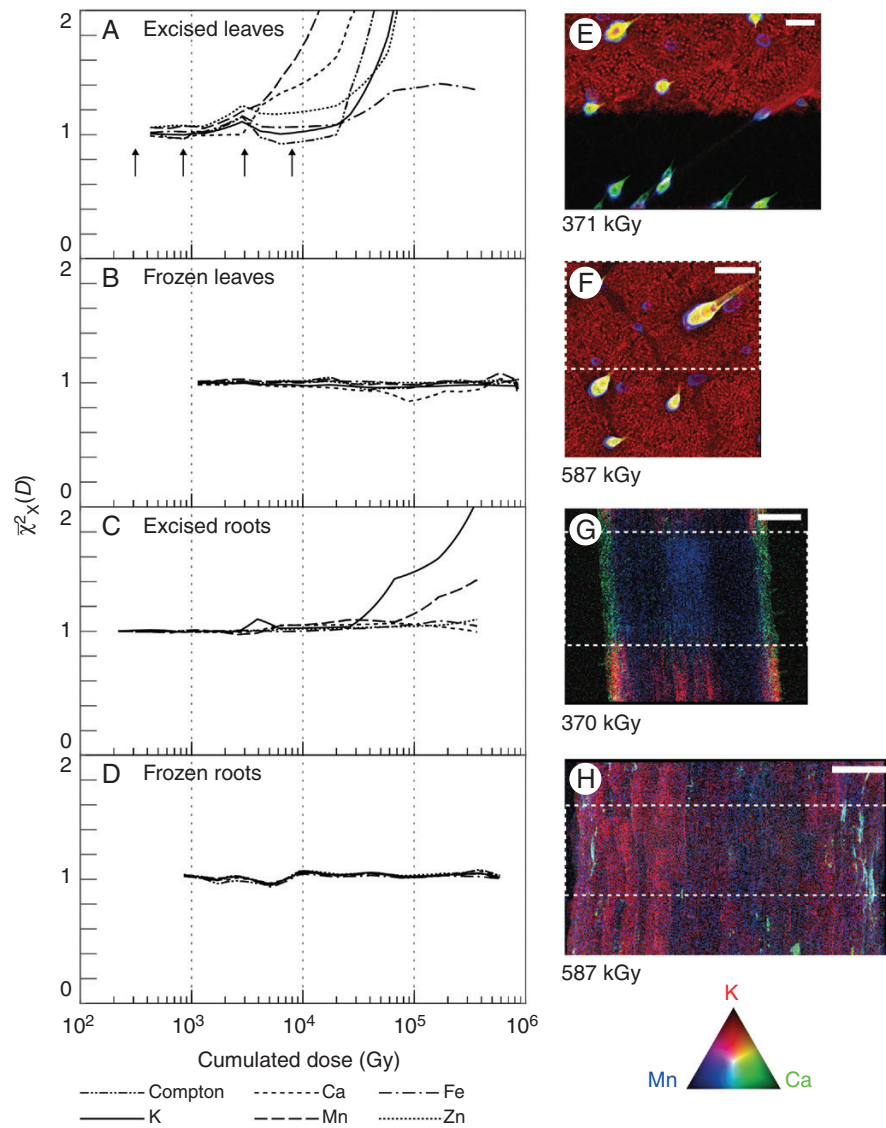
FIG. 2. Determination of X-ray-induced damage. Shown is the mean of the normalized global image change metric $\bar{\chi}_X^2(D)$ [eqn (2)] plotted for each measured analyte as a function of cumulative radiation dose (Gy) for (A) fresh leaves, (B) cryofixed leaves, (C) fresh roots and (D) cryofixed roots. Condensation on the fresh root specimen resulted in an inconsistent measure of Compton scatter, and it is therefore omitted from this case. Tri-colour images of K, Ca and Mn at the end of the damage cycle are shown for each specimen type (E–H). The damaged area is depicted by a white dashed box. The total accumulated dose is shown for each image with the colours encoded according to the RGB colour triangle. The scale bar in (E) is equal to 100 μm, and in (F–H) are equal to 200 μm. The four arrows in (A) refer to the doses delivered in Fig. 4.

TABLE 1. *Mean and s.d. of the damage threshold for fresh leaves (n = 3) and fresh roots (n = 2)*

	Damage threshold (kGy)			
Element	Leaves (fresh)	Roots (fresh)	*C. elegans* (fresh)	*C. elegans* (lyophilized)
Potassium	45.8 (7.67)	8.27 (3.68)	*	10×10^3
Calcium	14.1 (10.7)	†	*	30×10^3
Manganese	19.7 (14.8)	23.2 (*)	*	40×10^3
Iron	66.3 (‡)	†	1.5×10^3	40×10^3
Zinc	46.6 (7.36)	†	*	40×10^3

The damage threshold is defined as the point where the damage metric, $\overline{\overline{\chi_X^2}}$ [eqn (3)], for the sample deviates from 1 by ±0.5. Damage thresholds for *C. elegans* are shown for comparison (Jones *et al.*, 2017).

*Statistically limited.

†No damage observed.

‡Damage observed in only one specimen.

TABLE 2. *An approximate conversion guide from experimental parameters to radiation dose for hydrated plant specimens assuming the focus spot is oversampled*

Beamline type	Flux (photons s^{-1})	Pixel size (µm)	Dwell (ms)	Dose (Gy)
FZP* nanoprobe	10^9	0.05	100	1.5×10^7
KB† nanoprobe	10^{10}	0.1	2	7.4×10^5
KB‡ microprobe	10^{10}	2	2	1.8×10^3
In-house§	10^8	25	100	6.6

*Fresnel Zone Plate (e.g. BioNanoProbe, APS).

†Kirkpatrick–Baez mirror pair (e.g. P06, DESY).

‡Kirkpatrick–Baez mirror pair (e.g. XFM, Australian Synchrotron).
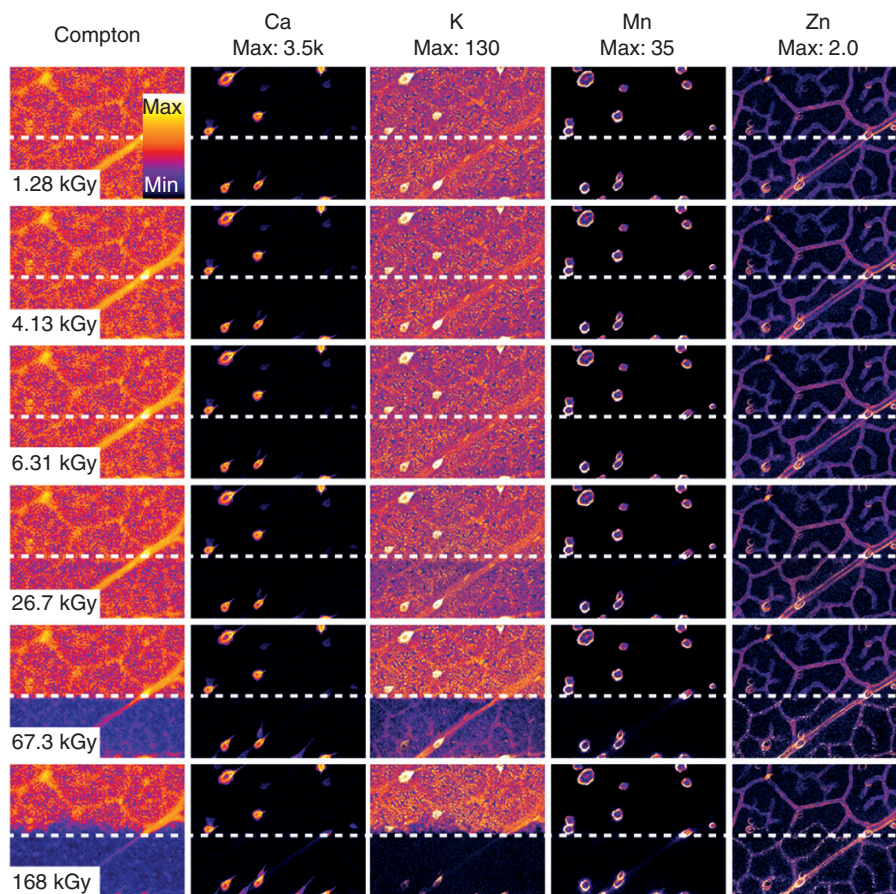
§In-house XFM (e.g. iXRF ATLAS system with Mo source).

FIG. 3. Visualization of radiation-induced damage for a single fresh leaf specimen (as presented in Fig. 2E) where each column represents the Compton scatter or a measured analyte, and each row represents a cumulative radiation dose. Here we see that for some elements the damage is obvious (K and Zn) while for others the changes are subtler (Ca and Mn) and only borne out by visualization of the $\chi^2(D)$ damage metric (Figs 4 and 5). The elemental concentration in each case is indicated for each column in units of µg cm^{-2} and is encoded according to the colour bar.

of 4.13 kGy (Fig. 4). The damage is localized to the trichome (white arrowheads in Fig. 4), with the background relatively unchanged. Radiation-induced damage in K was observed at a radiation dose of 6.31 and 26.7 kGy. Here, we begin to observe bulk changes in the specimen in the damage region, resulting in observed changes in all the measured elements. These radiation dose levels at which changes occur are in line with those observed in Fig. 2. In the leaves, Mn and Ca move when the trichomes are damaged, followed by water (and K) moving away as cell walls are broken. Eventually, when de-hydrated, elements deeper in the leaf tissue are exposed to radiation, although it is uncertain if this results from damage

or if the visibility changes. The reference part of the excised hydrated leaf is largely undamaged optically (at approx. 2.5 kGy dose) (Fig. 5A, B).

Radiation damage in excised (hydrated) roots

In addition to leaves, we set out to assess radiation damage limits in excised (hydrated) roots. Elemental maps of Mn and K together with maps of the $\chi^2(D)$ at two accumulated radiation dose levels for the same elements show radiation-induced damage in K at a radiation dose of 26.7
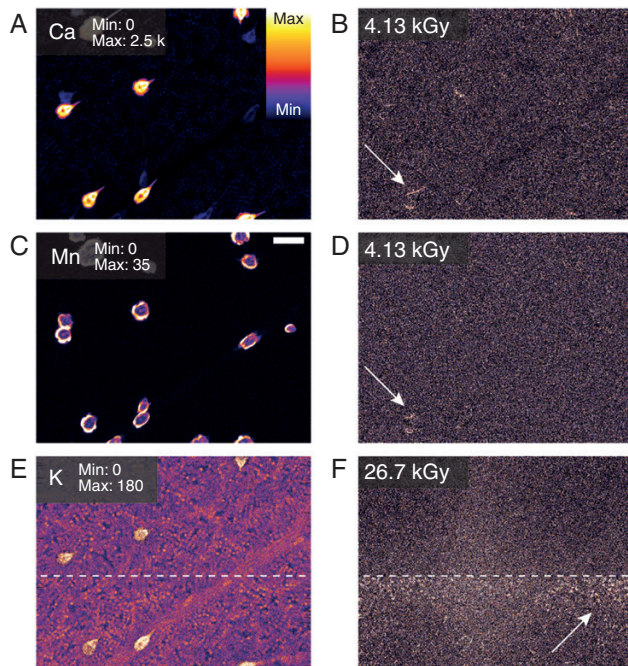
FIG. 4. Elemental maps of Ca (A), Mn (C) and K (E) together with maps of the χ^2 (D) at two accumulated radiation dose levels for the same elements in excised hydrated leaves. Here we see changes in the specimen for both Ca (B) and Mn (D) at a dose level of 4.13 kGy, while the first changes in K (E) are observed at a dose level of 26.7 kGy. The scale bar in (C) is equal to 100 μm. The range of displayed elemental areal density (μgcm⁻¹) is shown in (A), (C), and (E).

kGy (Fig. 6). Here, we begin to observe the first signs of dehydration in the specimen in the damaged region (i.e. mass loss) resulting in shrinkage. At a dose level of 67.1 kGy, we see changes in the specimen for Mn (Fig. 6), probably as a result of the previously mentioned dehydration, with the damage most readily visible in the cortex (white arrowheads in Fig. 6). The radiation dose levels at which these changes occur are in line with those observed in Fig. 2. Optical imaging after the experiment shows that the reference part of the excised hydrated root is largely undamaged optically (at approx. 2.5 kGy dose) (Fig. 5C, D); however, damage has begun to diffuse away from the area of most intense damage.

Radiation damage in excised (hydrated) cryogenic state

As reported previously (Beetz and Jacobsen, 2002; Jones *et al.*, 2017), cryofixed specimens (Fig. 2B, D) show no radiation-induced changes up to the maximum dose delivered, with no observable damage in either the calculated metric or the final reference image of the specimen. Cryogenic excised leaves show damage immediately visible upon thawing which is not evident while frozen compared with the XFM map at approx. 6–8 h after initial measurement (Fig. 5E, F). Unexpectedly, cryogenic excised roots did not show any visible damage upon thawing (Fig. 5G).

Time-dependent radiation-induced damage in leaves

The aim of this part of the study was to elucidate whether low X-ray doses result in damage at a later time as reported by Lombi *et al.* (2011). We split this experiment into two parts. In the first part we assessed the long-term damage to the specimen up to 9 d after receiving the radiation dose, particularly relevant for using XFM as an advanced phenotyping tool for characterizing plant accessions or mutants under a dose treatment. In the second part we examined changes on experimental time scales of the order of 10 min.

Long-term damage Areas of leaves of four separate living plants were given a radiation dose from 0.3 to 8.1 kGy. To assess damage during the 9 d post-scanning period, we used light microscopy as well as in-house XFM analysis at The University of Queensland. Of the four doses (0.3, 0.9, 3.0 and 8.1 kGy) delivered to the living plants, only the leaf area dosed at 0.3 kGy did not show symptoms of radiation damage after 2–9 d and with the elemental maps acquired after 9 d not showing any damage (Fig. 7). The leaf area exposed to 0.9 kGy did not have any visible symptoms immediately after XFM analysis, but a very slight discoloration was evident after 2 d, with this becoming more severe by 9 d. The element maps acquired after 9 d had slightly reduced K concentrations. The leaf areas exposed to 3.0 and 8.1 kGy doses had only minor damage visible using light microscopy immediately after XFM analysis, but the severity of this damage increased markedly from 2 to 9 d. In the case of the 3.0 kGy-dosed leaf area, mild discoloration was visible after 2 d, followed by bleaching after 5 d and browning after 9 d. The elemental maps acquired after 9 d show that K, Ca or Mn have been removed from the damaged area. In the case of the 8.1 kGy-dosed leaf area, blackening (possibly due to free radicals carbonizing cellulose) is visible after 2 d. After 5 and 9 d, the area is completely dead and consists of a cellulose matrix with K removed, but Mn and Ca (in trichomes) are locked in place (Fig. 7).

Short-term damage To assess the short-term effects of radiation damage, for example when imaging a specimen multiple times such as an overview image followed by several detailed area studies, we imaged small areas separated by 10 min, followed by an image after an additional 1 min. In order to image on short time scales, the imaging area had to be reduced, making visual and statistical analysis problematic. In this case, we use the total K signal as a proxy for mass loss, and track the K over each image. The results presented in Fig. 8 show that for low to moderate imaging doses (approx. 2 kGy), about 5 % of the K signal has been lost after 10 min. However, at higher radiation dose (approx. 8 kGy), significant loss (>15 %) of the K signal is observed. These results confirm the findings from the long-term radiation damage observations in Fig. 7 which suggests that significant damage occurs at a radiation dose between 0.9 and 3.0 kGy. Using the results of the short-term study, we can refine the lower bound, with minimal damage occurring at a radiation dose of 2.1 kGy (Fig. 8A). These results demonstrate that the damage observed in Fig. 7 occurs on a time scale of minutes, but may not be immediately apparent.
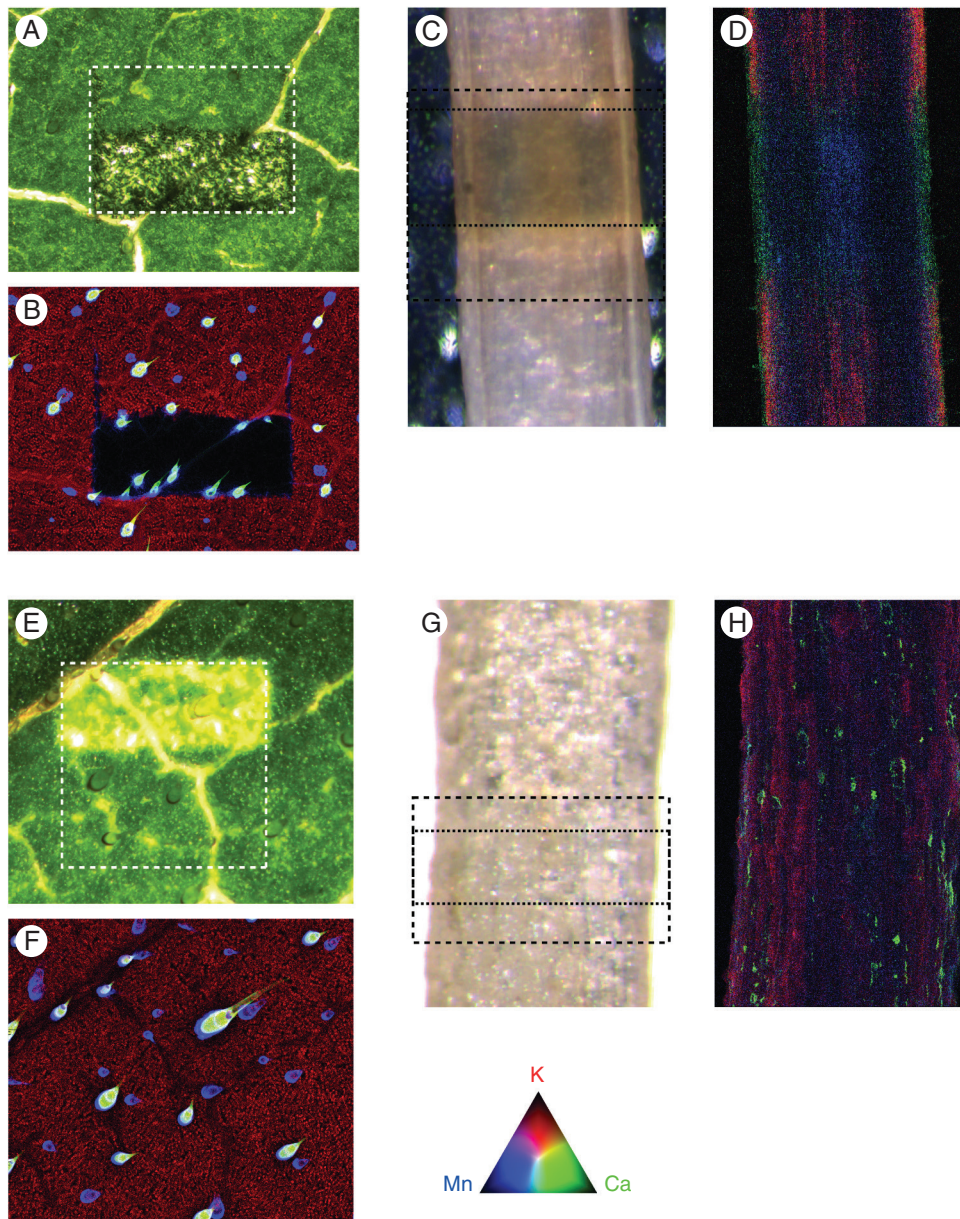
FIG. 5. Optical microscope images of each specimen immediately after being removed from the beamline, together with the final XFM overview image. Fresh leaves (A, B) and fresh roots (C, D) show damage in both the optical and fluorescence images, with the damage in the fresh root extending beyond the damaged region. Frozen leaves (E, F) and frozen roots (G, H) show no damage in the final XFM image, but damage appears once thawed in the leaf but not the root. In each case, the reference area is shown with a dashed box, and in (C) and (G) the damage area is also shown with the dotted box. The colours for the XFM images are encoded according to the colour triangle.

DISCUSSION

The ultimate aim of XFM as a tool for the study of physiological processes taking place in plants is to examine these processes at a particular moment in time (or multiple moments in time), as close as possible to the natural state of the plant (van der Ent *et al.*, 2017). 'Damage' then can be defined as any change to the specimen that compromises the examination of these processes. This study has shown that element-specific redistribution and breakdown of localized structures can occur at doses routinely in use at XFM beamlines. Importantly, although radiation effects in excised specimens became obvious

between 26.7 and 67.3 kGy, subtle redistribution of soluble elements was detectable even at 4.13 kGy, equivalent to a dwell time of only 5 ms on a KB-microprobe beamline (Table 2). Moreover, although gross changes are apparent when comparing the area of damage with the reference in our study, there is no guarantee that even the differences at 26.7 kGy would be obvious to a researcher looking only at the damaged area. Indeed, Lombi *et al.* (2011) only observed radiation-induced damage once it became significant at a dose of the order of 200 kGy.

Fittschen *et al.* (2017) report that at a radiation dose of approx. 100 Gy photosynthetic function is reduced in

Arabidopsis thaliana, suggesting cellular damage, while photosynthetic function was not affected at lower doses (approx. 6 Gy). However, the present study suggests that a dose of 100 Gy
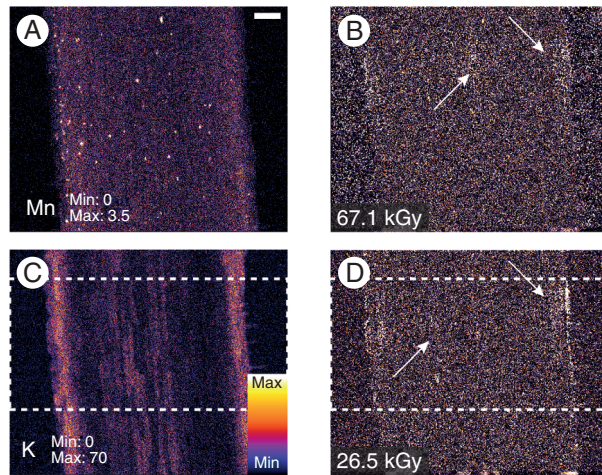

FIG. 6. Elemental maps of Mn (A) and K (C) together with maps of the χ^2 (D) at two accumulated radiation dose levels for the same elements in excised (hydrated) roots. Here we see changes in the specimen for both Mn (B) and K (D) at dose levels of 67.1 kGy and 26.5 kGy, respectively. Damage is identified with white arrows, with the damage region approximated with the dashed white boxes in (C) and (D). The scale bar in (A) is equal to 100 μm.

does not result in long- or short-term elemental redistribution, and that at this dose the visible health of the plant is unaffected up to 9 d post-irradiation (Fig. 7). These doses appear far lower than those reported by Jones *et al.* (2017) for *C. elegans*, where damage was found only at doses in excess of 1 MGy for fresh specimens and >10 MGy for freeze-dried specimens, highlighting the specimen-dependent damage limits. Indeed Lu *et al.* (2013) do not report any radiation damage to rice seeds at doses of approx. 7 MGy.

It is notable that damage-related effects were seen to occur at different rates for different elements. Highly diffusible ions, such as solute K within vacuoles or solute Ca at the base of the sunflower trichomes, disperse due to breakdown of the vacuolar membrane, even at a low radiation dose. In contrast, non-diffusible ions, such as Si or insoluble Ca in crystalline deposits, may be unaffected even at a high radiation dose. Consequently, if the main objective of a study is to reveal K distribution or that of other diffusible ions such as Na, Rb, Cs, Cl or Br in vacuoles, radiation doses must be kept low. Conversely, if the objective is to reveal localization of Si or crystalline Ca in trichomes or in Ca oxalate crystals, higher radiation doses may be considered. While this study sought to establish thresholds for changes in distribution (i.e. mass loss or movement), it is expected that changes to chemical speciation would occur at even lower doses, and any study seeking such information would need to adhere to even more conservative thresholds.
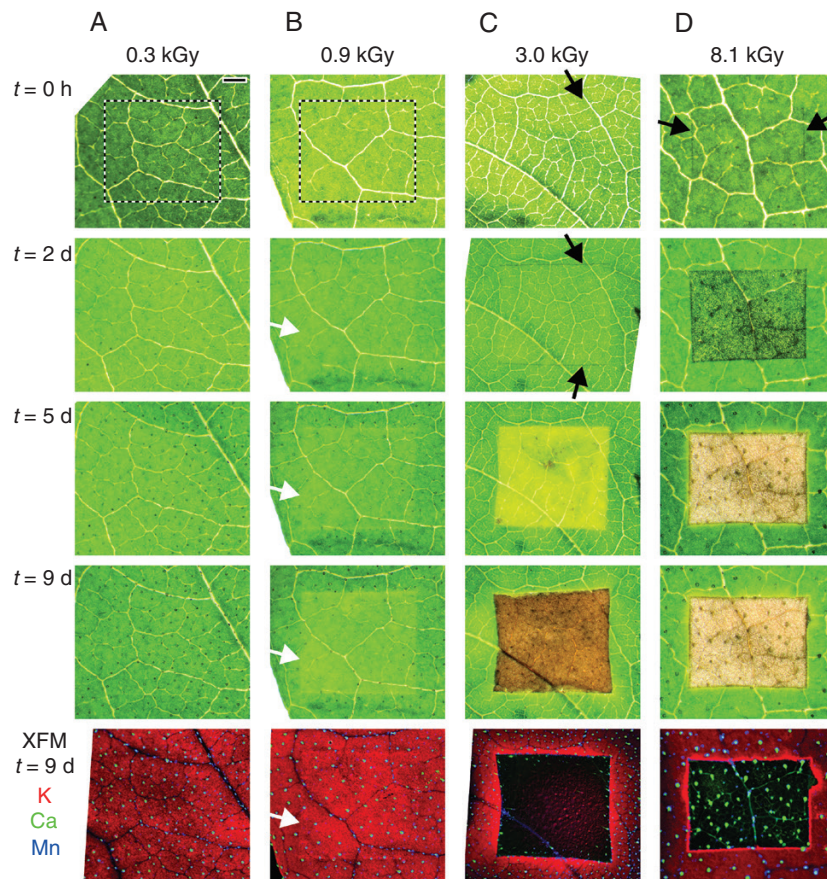

FIG. 7. Living leaves given increasing X-ray radiation doses (columns A–D) and then optically imaged immediately after dosing and at regular intervals afterwards (t = 2, 5 and 9 d). After 1 week, leaves were imaged using an in-house XFM system, with an RGB composite with red, green and blue representing K, Mn and Ca, respectively. The colours mix according to the colour triangle in Fig. 1. The scale bar in (A) is equal to 1 mm, and the dose delivered in each case is indicated with four vertical arrows in Fig. 1A.
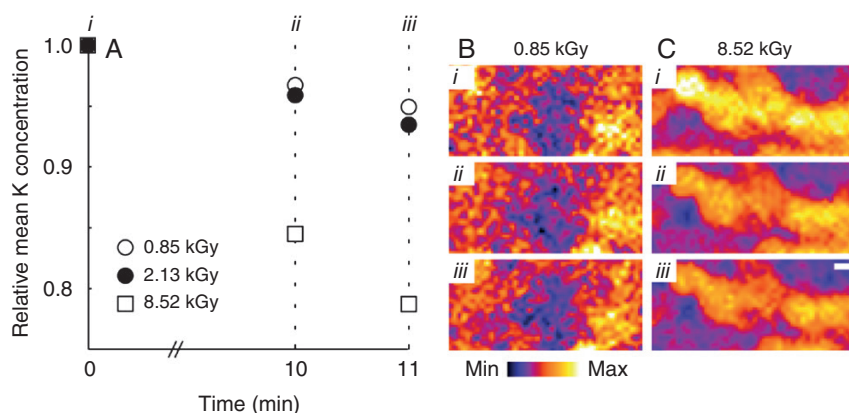
Fig. 8. Repeated measurements of a small area in rapid succession highlight the time dependence of radiation-induced damage. Using the K signal as a proxy for mass loss, we see that after three repeated images of 852 Gy separated by 10 min and an additional 1 min, approx. 95 % of the total K is present, with similar results observed for a dose of 2.13 kGy (A). However, increasing the imaging dose to 8.52 kGy results in significant (>15 %) loss in the K signal after 10 min (B and C).

A complicating factor is that many studies report on the incident beam energy (keV) and dwell time (ms), but often not the critical parameter: X-ray flux at the specimen. Without a record of the incident flux, it is impossible to assess the dose experienced by the specimen and therefore the likelihood of damage affecting the results.

These results also highlight the time-dependent nature of radiation damage, suggesting that particular care should be taken in longer experiments. In the extreme case, radiation-dosed leaves attached to live plants were grown for a further 9 d and re-measured using in-house XFM to evaluate longer term radiation dose effects. The areas that were irradiated continued to develop bleaching and necrosis in the hours and days after exposure, probably due to reactive free radicals, with post-dose elemental redistribution observed even at 0.9 kGy, equivalent to as little as 1 ms dwell on a KB-microprobe beamline (Table 2). Even at much shorter time scales, such as the minutes to hours intervals within a sequence of scans, redistribution of elements may continue to occur for some time after the dose has been delivered. Indeed, a dose of 8.5 kGy was sufficient to cause a 15 % loss of K after only 10 min (Fig. 8). Consequently, any studies in which a living specimen is scanned repeatedly over time to examine the kinetics of elemental changes (Blamey *et al.*, 2018; Doolette *et al.*, 2018) should be careful to address the possibility that any time-dependent changes are due to damage and not the desired physiological effect.

Recent advances in detection efficiency such as annular arrays, however, measure a greater number of fluorescence events relative to incident photons and therefore improve sensitivity and reduce the dose required for imaging. Imminent improvements in detector electronics, such as the SDD version of the Maia detector (Chen *et al.*, 2017) and the four-pixel SDD array (Rococo 3, PNDetector, Germany) are poised to deliver further advances on this front. Recently Blamey *et al.* (2018) undertook a time-dependent study taking advantage of recent advances in detection and scanning technology. They imaged cowpea leaves repeatedly over 48 h, with an approximate radiation dose of 50 Gy (1.3×10^5 photons μm^{-2}) per image, giving a total accumulated radiation dose of approx. 300 Gy, below the threshold where long- or short-term radiation damage is apparent (Figs 7 and 8).

Though not suited to *in vivo* studies, cryogenic analysis in the frozen-hydrated state emerges as a key damage mitigation strategy. This has long been considered the 'gold standard' for microanalytical investigations of plant tissues as it is assumed *a priori* to preserve intrinsic element distribution and chemical form indefinitely (van der Ent *et al.*, 2017). Bearing this out, frozen-hydrated samples in this study did not incur any apparent damage even at high doses (e.g. 587 kGy). This may be explained by the complete immobilization of entrained water limiting induced analyte movement and hence elemental redistribution. However, few XFM beamlines have cryogenic capabilities beyond a nitrogen cryostream (suitable only for very small specimens, <2 × 2 mm). The extreme radiation hardness of plant tissues in the cryogenic state has important implications for studies where a high radiation dose is inevitable, such as high-resolution nanoprobes (Table 2) and in XANES mapping and tomography. It has long been assumed that cryogenic freezing gives a sufficient level of protection from the effects of radiation damage for XANES imaging. However, this hypothesis has not been systematically tested for plants, and freezing at −195 °C in liquid nitrogen does not prevent chemical bond breaking (Beetz and Jacobsen, 2002).

Minimization of dose is the most obvious means of reducing damage. However, it is clear that radiation damage is dependent on specimen characteristics, such as hydration state, bulk composition, density, etc., and will therefore vary from specimen to specimen. The results of this study show that damage occurs at very low doses, and that localized disintegration of structures and element-specific redistribution occur, with more mobile elements changing first. We suggest that experiments on hydrated specimens are best designed with dose as a key consideration. Fast, low-dose scans on adjacent areas can be reported as simple references (Blamey *et al.*, 2018), and it is important to avoid dwell times that are excessive for the sensitivity required. In the absence of available measurements of the incident X-ray flux, Table 2 can be used to estimate the radiation dose delivered to the specimen, and eqn (1) can be used to calculate the dose directly. Taking an upper limit of the tolerable radiation dose as 4 kGy for a single image, dwell time and beam size can be used to adjust and minimize the delivered radiation dose. Ultimately, the sensitivity of the microscope to the

element of interest places a lower limit on the dose delivered to the specimen.

Altogether, it is apparent that elemental redistribution occurs at a dose lower than visible damage, and this has important implications. It is critical that researchers explicitly consider the development of artefacts due to elemental redistribution, and, at a minimum, where damage is visible in light micrographs it should be considered that elemental redistribution has already occurred. We have shown that the relationship between flux, dose, time and damage is particular to the system under investigation. The results from this study will enable plant scientists to make informed decisions when designing experiments, and serve as a reference for the X-ray fluorescence community in terms of XFM analysis of plants.

ACKNOWLEDGEMENTS

LITERATURE CITED

Beetz T. Jacobsen C. 2002. Soft X-ray radiation-damage studies in PMMA using a cryo-STXM. *Journal of Synchrotron Radiation* **10**: 280–283.

Blamey FPC, Hernandez-Soriano MC, Cheng M, *et al.* 2015. Synchrotron-based techniques shed light on mechanisms of plant sensitivity and tolerance to high manganese in the root environment. *Plant Physiology* **169**: 2006–2020.

Blamey FPC, Paterson DJ, Walsh A, *et al.* 2018. Time-resolved X-ray fluorescence analysis of element distribution and concentration in living plants: an example using manganese toxicity in cowpea leaves. *Environmental and Experimental Botany* **156**: 151–160.

Budka D, Mesjasz-Przybylowicz J, Przybylowicz WJ. 2004. Micro-PIXE analysis: importance of biological sample preparation techniques. *Radiation Physics and Chemistry* **71**: 785–786.

Budka D, Mesjasz-Przybylowicz J, Tylko G, Przybylowicz WJ. 2005. Freeze-substitution methods for Ni localization and quantitative analysis in *Berkheya coddii* leaves by means of PIXE. *Nuclear Instruments and Methods in Physics Research Section B: Beam Interactions with Materials and Atoms* **231**: 338–344.

Chen W, Elliott D, Giacomini G, Kusczewski AJ, *et al.* 2017. Improvement of SDD-Maia detector for X-ray fluorescence detection. In: *Nuclear Science Symposium and Medical Imaging Conference.* doi: 10.1109/nssmic.2017.8532602.

Doolette CL, Read TL, Li C, *et al.* 2018. Foliar application of zinc sulfate and zinc EDTA to wheat leaves: differences in mobility, distribution and speciation. *Journal of Experimental Botany* **69**: 4469–4481.

van der Ent A, Przybylowicz WJ, de Jonge MD, *et al.* 2017. X-ray elemental mapping techniques for elucidating the ecophysiology of hyperaccumulator plants. *New Phytologist* **218**: 432–452.

Fittschen UEA, Kunz HH, Höhner R, Tyssebotn IMB, Fittschen A. 2017. A new micro X-ray fluorescence spectrometer for in vivo elemental analysis in plants. *X-Ray Spectrometry* **46**: 374–381.

Gianoncelli A, Vaccari L, Kourousias G, *et al.* 2015. Soft X-ray microscopy radiation damage on fixed cells investigated with synchrotron radiation FTIR microscopy. *Scientific Reports* **5**: 10250. doi: 10.1038/srep10250.

Hackett MJ, Hollings A, Caine S, *et al.* 2019. Elemental characterisation of the pyramidal neuron layer within the rat and mouse hippocampus. *Metallomics* **11**: 151–165.

Hare DJ, New EJ, De Jonge MD, McColl G. 2015. Imaging metals in biology: balancing sensitivity, selectivity and spatial resolution. *Chemical Society Reviews* **44**: 5941–5958.

James SA, Hare DJ, Jenkins NL, de Jonge MD, Bush AI, McColl G. 2016. φXANES: *in vivo* imaging of metal–protein coordination environments. *Scientific Reports* **6**: 20350. doi: 10.1038/srep20350.

Jones MWM, Hare DJ, James SA, de Jonge MD, McColl G. 2017. Radiation dose limits for bioanalytical X-ray fluorescence microscopy. *Analytical Chemistry* **89**: 12168–12175.

de Jonge MD, Holzner C, Baines SB, *et al.* 2010. Quantitative 3D elemental microtomography of *Cyclotella meneghiniana* at 400 nm resolution. *Proceedings of the National Academy of Sciences, USA* **107**: 15676–15680.

de Jonge MD, Vogt S. 2010. Hard X-ray fluorescence tomography – an emerging tool for structural visualization. *Current Opinion in Structural Biology* **20**: 606–614.

Kachenko AG, Siegele R, Bhatia NP, Ionescu M. 2008. Evaluation of specimen preparation techniques for micro-PIXE localisation of elements in hyperaccumulating plants. *Nuclear Instruments and Methods in Physics Research Section B: Beam Interactions with Materials and Atoms* **266**: 1598–1604.

Kirkham R, Dunn PA, Kuczewski AJ, *et al.* 2010. The Maia spectroscopy detector system: engineering for integrated pulse capture, low latency scanning and realtime processing. *AIP Conference Proceedings* **1234**: 240–243.

Kirz J, Jacobsen C, Howells MR. 1995. Soft X-ray microscopes and their biological applications. *Quarterly Reviews of Biophysics* **28**: 33–130.

Kopittke PM, Blamey FPC, Asher CJ, Menzies NW. 2010. Trace metal phytotoxicity in solution culture: a review. *Journal of Experimental Botany* **61**: 945–954.

Kopittke PM, Menzies NW, de Jonge MD, *et al.* 2011. In situ distribution and speciation of toxic copper, nickel, and zinc in hydrated roots of cowpea. *Plant Physiology* **156**: 663–673.

Kopittke PM, de Jonge MD, Wang P, *et al.* 2014. Laterally resolved speciation of arsenic in roots of wheat and rice using fluorescence-XANES imaging. *New Phytologist* **201**: 1251–1262.

Kopittke PM, Punshon T, Paterson DJ, *et al.* 2018. Synchrotron-based X-ray fluorescence microscopy as a technique for imaging of elements in plants. *Plant Physiology* **178**: 507–523.

Kosior E, Cloetens P, Deves G, Ortega R, Bohic S. 2012. Study of radiation effects on the cell structure and evaluation of the dose delivered by x-ray and α-particles microscopy. *Applied Physics Letters* **101**: 263102.

Larabell CA, Le Gros MA. 2004. X-ray tomography generates 3-D reconstructions of the yeast, *Saccharomyces cervisia*e, at 60-nm resolution. *Molecular Biology of the Cell* **15**: 957–962.

Li C, Wang P, van der Ent A, *et al.* 2019. Absorption of foliar-applied Zn in sunflower (*Helianthus annuus*): importance of the cuticle, stomata and trichomes. *Annals of Botany* **123**: 57–68.

Lombi E, de Jonge MD, Donner E, *et al.* 2011. Fast X-ray fluorescence microtomography of hydrated biological samples. *PLoS One* **6**: e20626. doi: 10.1371/journal.pone.0020626.

Lu L, Tian S, Liao H, *et al.* 2013. Analysis of metal element distributions in rice (*Oryza sativ*a L.) seeds and relocation during germination based on X-ray fluorescence imaging of Zn, Fe, K, Ca, and Mn. *PLoS One* **8**: e57360. doi: 10.1371/journal.pone.0057360.

Paterson D, de Jonge MD, Howard DL, *et al.* 2011. The X-ray fluorescence microscopy beamline at the Australian Synchrotron. *AIP Conference Proceedings* **1365**: 219–222.

Ryan CG, van Achterbergh E, Yeats CJ, Win TT, Cripps G. 2002. Quantitative PIXE trace element imaging of minerals using the new CSIRO–GEMOC nuclear microprobe. *Nuclear Instruments & Methods in Physics Research, Section B: Beam Interactions with Materials and Atoms* **189**: 400–407.

Ryan CG, Siddons DP, Kirkham R, *et al.* 2014. Maia X-ray fluorescence imaging: capturing detail in complex natural samples. *Journal of Physics: Conference Series* **499**: http://iopscience.iop.org/article/10.1088/1742-6596/499/1/012002/meta.

Ryan CG, Kirkham R, de Jonge MD, *et al.* 2018. The Maia detector and event mode. *Synchrotron Radiation News* **31**: 21–27.

Scheckel KG, Lombi E, Rock SA, McLaughlin MJ. 2004. In vivo synchrotron study of thallium speciation and compartmentation in *Iberis intermedia*. *Environmental Science and Technology* **38**: 5095–5100.

Siddons DP, Kirkham R, Ryan CG, *et al.* 2014. Maia X-ray microprobe detector array system. *Journal of Physics: Conference Series* **499**: 012001.

Turnau K, Przybylowicz WJ, Mesjasz-Przybylowicz J. 2001. Heavy metal distribution in *Suillus luteus* mycorrhizas – as revealed by micro-PIXE analysis. *Nuclear Instruments and Methods in Physics Research B* **181**: 649–658.

Warley A. 1997. *X-ray microanalysis for biologists.* London: Portland Press Ltd.

Weiß D, Schneider G, Niemann B, Guttmann P, Rudolph D, Schmahl G. 2000. Computed tomography of cryogenic biological specimens based on X-ray microscopic images. *Ultramicroscopy* **84**: 185–197.